

Waveform analysis of Scholte modes in ocean sediment layers

Guust Nolet¹ and LeRoy M. Dorman²

¹Department of Geological and Geophysical Sciences, Princeton University, Princeton, NJ 08544, USA

²Scripps Institution of Oceanography, UCSD, 9500 Gilman Drive, La Jolla, CA 92093–0215, USA

Accepted 1995 November 3. Received 1995 November 3; in original form 1995 March 27

SUMMARY

In an effort to determine the characteristics of seismic noise on the ocean bottom and its relationship to the structure of the sea-floor, we have adapted the method of non-linear waveform fitting to accommodate multidimensional models (shear velocity β and shear damping Q_S), and have applied it to invert several records of interface waves (Scholte 1958) from the THUMPER experiment off southern California. Waveform fitting is a very powerful tool to determine the S velocity in the top few metres of the sediment. Starting from $\beta = 30 \text{ m s}^{-1}$ at the top clay layer, the S velocity increases with a gradient of $2.8 \text{ m s}^{-1} \text{ m}^{-1}$ over the first 150 m of sediment. A theoretical estimation of the source strength gives coherent estimates of Q_S as a function of depth for distances between 400 and 1070 m from the source. The Q_S models are characterized by very low values (10–20) in the top three metres, but by values in excess of 100 below that level. The results confirm the identification of the noise as harmonics of interface waves. In the area of this experiment, the largest noise amplitudes belong to the fundamental mode and penetrate to a depth of about 20 m into the sediment. The overtone energy can be appreciable too, and is noticeable to about 80 m depth. The Q_S structure confirms the strong influence that the sea-floor structure has on the noise spectrum. The high attenuation at frequencies above 3–4 Hz suppresses noise propagation and produces low noise at higher frequencies. (Similarly, high attenuation in the asthenosphere suppresses noise propagation below 0.1 Hz.)

Key words: attenuation, guided waves, sediments, waveform analysis.

INTRODUCTION

At present, OBSs (ocean-bottom seismometers) are an important practical means of obtaining seismological data at the sea-floor, and considerable attention has been paid in recent years to the noise characteristics of OBS recordings and their relationship to the shear-velocity structure at the sea bottom (e.g. Dorman, Schreiner & Bibee 1991).

In the deep oceans, the soil conditions we find are very different from those on the continents or their margins. Continental sources of solids (except for fine wind-blown components) are confined to the edges of continents, so most of the sediment reaching the central portions of the ocean basins is detritus from the plants and animals living above. The volume of these biogenic sediments is about 30 per cent of the total, although about 55 per cent of the area of the sea-floor is dominantly biogenic (Seibold & Berger 1993). Chemically, the biogenic sediments may be carbonate-based (calcareous) or silicate-based (siliceous).

The sedimentation rate for calcareous sediments is typically an order of magnitude higher than that for siliceous sediments. The distribution of the two types on the sea-floor is controlled

primarily by the solubility of the carbonates, which increases with pressure and with acidity (dissolved CO_2), balanced by the accumulation rate of carbonates. The depth at which CO_2 dissolution exceeds accumulation is called the calcite compensation depth (CCD). Below the CCD, the predominant sediments will be siliceous oozes and wind-transported clays. In the equatorial regions, where the biological productivity is high, oozes dominate; elsewhere, clays will prevail. Thus, for most areas deeper than the CCD (3800–5000 m), the sediments are predominantly fine-grained silicates. As the CO_2 content of the atmosphere increases, the carbonate compensation depth (CCD) will rise.

The circulation of deep water in the ocean basins appears to be the most important factor controlling the CCD. In the North Atlantic, the bottom water is the North Atlantic Deep Water, which is young and has not yet absorbed much CO_2 . This condition lowers the CCD to ~ 5.5 km. The older, CO_2 -rich and chemically aggressive Antarctic Bottom Water, which fills the Pacific Basin, raises the CCD there to approximately the 4 km range. The CCD is locally depressed in the equatorial regions by the high supply of carbonates.

For teleseismic body waves, the noise spectrum around 1 Hz

is of particular importance. Schreiner & Dorman (1990) used an array of OBSs to observe the noise field in the 0.5–5 Hz frequency band and determined from the coherence characteristics that the ocean-floor noise consists of low-order modes of interface waves on the ocean bottom. Since these are waves on a fluid/solid interface, we shall use the term ‘Scholte waves’.¹

Scholte waves penetrate the very soft sedimentary layer, where the S velocity is below 200 m s^{-1} and where the P velocity is close to the speed of sound in water (around 1500 m s^{-1}). Schreiner, Dorman & Bibee (1991) determined the shear-wave velocity structure at two deep ocean sites off the coast of California. Their analysis used frequency-time filtering (Dziewonski & Hales 1972) to obtain group-velocity characteristics from waves generated by explosions at or very near the ocean bottom. In general, they were able to obtain good fits to the fundamental-mode group velocity. However, their model predicts first and second overtones at velocities that are different from those observed on some of the records.

This paper is an attempt to obtain a better understanding of the behaviour of the interface wave and the sediment structure by analysing the full waveforms. To this end, we shall use techniques of non-linear waveform inversion originally developed for long-period teleseismic waves. This paper therefore also represents an attempt to assess the feasibility of waveform fitting at high frequencies. Because of the importance of finding Q_S in addition to the S velocity, we shall redefine the damping strategy for finding optimum (minimum norm) models of more than one physical parameter.

Caiti, Akal & Stoll (1991) estimated shear attenuation by first inverting for wave dispersion and then comparing synthetic seismograms for the resulting velocity model but with different attenuation profiles. Our approach differs from their scheme in that we invert concurrently for both attenuation and shear velocity by directly fitting waveforms in the time domain. Ewing *et al.* (1992) obtained time-domain waveform fits for signals at close range in shallow water, apparently by trial and error rather than by non-linear optimization as in this study. Bromirski, Frazer & Duenebier (1992) measured sea-floor shear velocity and Q by using sea-floor–basement traveltime and attenuation measurements. In our case, the Scholte wave propagation is strongly affected by a thin (<10 m thick) layer which would not be distinguished by the interval methods.

NON-LINEAR WAVEFORM INVERSION

Nolet, van Trier & Huisman (1986) and Nolet (1990) described the application of non-linear optimization to the problem of

¹The terminology in use for interface waves differs amongst the various investigators. Jensen *et al.* (1994) reserve the term ‘Scholte wave’ for the fundamental mode on a solid–fluid interface, ‘Rayleigh wave’ for modes at the free surface of a solid, and propose to use ‘shear modes M1, M2...’ for the higher modes at the fluid–solid interface. However, the terms M1, M2 are strongly connected with theoretical solutions in simple two-layer models. In global seismology, this terminology disappeared in the 1970s, when the models became more and more complex, and the term ‘Rayleigh waves’ is now applied to all P – SV type modes, irrespective of the existence of an oceanic layer. Confusingly, Scholte (1958) refers to ‘his’ waves as ‘Rayleigh’ waves. Normal modes with energy concentrated at the core–mantle boundary are commonly said to lie on the ‘Stoneley branch’, even though this is a solid–fluid boundary that was extensively studied by Scholte (1956). We shall use the term ‘Scholte waves’ for all modes that have energy concentrated at the solid–liquid interface of the ocean bottom. This terminology is also used by Rauch (1980).

fitting seismic waveforms. We shall use these techniques to fit theoretical predictions of the signal at the ocean bottom. The method is summarized in this section.

This misfit of the signal is quantified by an objective function, given by

$$F(\mathbf{p}) = \int_{\mathcal{P}} |Rd(t) - Ru(t; \mathbf{p})|^v dt, \quad (1)$$

where \mathbf{p} is a vector of discrete model parameters, R an operator describing all windowing and filtering operations applied to the data d and the synthetics u , and where v is the Lebesgue norm, for which we use 2 in this study. Both a conjugate gradient scheme and Newton iteration are used to find the optimum model \mathbf{p}^{opt} that minimizes F .

The synthetics are generated by summing the first M modes in the frequency domain:

$$U(\omega; \mathbf{p}) = \sum_{m=1}^M A_m(\omega) H_0^{(2)}[k_m(\omega; \mathbf{p})x], \quad (2)$$

where $H_0^{(2)}[kx]$ is the Hankel function of the second kind, and where $k_m(\omega; \mathbf{p})$ is the wavenumber of mode m evaluated for model \mathbf{p} . To compute k_m , we use perturbation theory to find $\delta k_m(\omega; \mathbf{p})$ where δk is a perturbation to the wavenumber $k^{(0)}(\omega)$ evaluated for the background model.

The discrete model parameters p_1, p_2, \dots, p_N are the coefficients of a continuous model representation $\mathbf{m}(z)$ when projected on a set of basis functions $h_i(z)$. In this paper, we shall allow for depth-dependent continuous models represented by more than one physical parameter. In general,

$$\mathbf{m}(z) = \begin{bmatrix} \alpha(z) & \beta(z) & \rho(z) & q(z) \\ \alpha_0 & \beta_0 & \rho_0 & q_0 \end{bmatrix}, \quad (3)$$

where α is the compressional velocity, β the shear velocity, ρ the density, and $q = Q_S^{-1}$ the inverse of the shear quality factor Q_S . All are dependent on depth z . The zero-subscripted quantities are scaling factors; these can be chosen equal to some average value of the physical parameter or, if a Bayesian approach to inversion is preferred, to the average *a priori* uncertainty of the model parameter. In general, we formulate the inverse problem in terms of perturbations $\delta\mathbf{m}$ with respect to the background model \mathbf{m} , and \mathbf{p} parametrizes $\delta\mathbf{m}$ rather than the full model. The scaling influences the damping of the model, or the choice of model through the minimization of $|\delta\mathbf{m}|^2$ if the inverse problem is underdetermined. The discrete parameters p_i can be viewed as constants for some interpolation scheme. We can always write the interpolation scheme in terms of basis functions $h_i(z)$: for example,

$$\delta\alpha(z) = \sum_{i=1}^N p_i h_i(z). \quad (4)$$

The functions $h_i(z)$ have a boxcar shape if we deal with simple layered models, as in this paper. They would be locally linear functions of z for linear interpolation schemes, or polynomials for higher-order schemes such as spline interpolation. For multidimensional models, we shall often wish to couple the changes in various parameters, for example by using Birch’s relationship between velocity and density. A convenient way to accommodate this is to amend (4), and write the change in the model as

$$\delta\mathbf{m} = \sum_{i=1}^N \begin{bmatrix} \frac{c_{\alpha i}}{\alpha_0} p_i h_i(z), & \frac{c_{\beta i}}{\beta_0} p_i h_i(z), & \frac{c_{\rho i}}{\rho_0} p_i h_i(z), & \frac{c_{q i}}{q_0} p_i h_i(z) \end{bmatrix}. \quad (5)$$

The vector of coefficients $\mathbf{c}_i \equiv (c_{\alpha i}, c_{\beta i}, c_{\rho i}, c_{q i})$ governs the contribution of each of the physical model variables to the i th parameter. If more than one c_i is non-zero, parameters are coupled in the inversion.

Nolet (1990) shows how a second-order expansion of $F(\mathbf{p})$ allows us to transform the discrete model parameters p_i to a set of uncorrelated parameters η_i with known variances. To this end, we compute the elements of the Hessian matrix, defined by $H_{ij} = \partial^2 F / \partial p_i \partial p_j$ with finite differences, and expand:

$$F(\mathbf{p}) \approx F(\mathbf{p}_{\text{opt}}) + \frac{1}{2}(\mathbf{p} - \mathbf{p}_{\text{opt}})^T \mathbf{H}(\mathbf{p} - \mathbf{p}_{\text{opt}}). \quad (6)$$

\mathbf{H} can be diagonalized:

$$\mathbf{H} = \mathbf{S} \mathbf{\Lambda} \mathbf{S}^T. \quad (7)$$

We define a set of new discrete model parameters η_i :

$$\boldsymbol{\eta} = \mathbf{S}^T \mathbf{p}. \quad (8)$$

Since \mathbf{H} is symmetric, \mathbf{S} is orthonormal and $\mathbf{p} = \mathbf{S} \boldsymbol{\eta}$. We use our subjective opinion to define how far F can rise above its minimum value without violating 'good fit' to the waveforms. If F is allowed to deviate by an amount ε from its minimum value at $F(\mathbf{p}_{\text{opt}})$, we define a confidence region $\Delta \mathbf{p} = \mathbf{p} - \mathbf{p}_{\text{opt}}$ by

$$\frac{1}{2} \Delta \mathbf{p}^T \mathbf{H} \Delta \mathbf{p} < \varepsilon. \quad (9)$$

This implies, for the transformed parameters, that $\Delta \boldsymbol{\eta}^T \mathbf{\Lambda} \Delta \boldsymbol{\eta} / 2 < \varepsilon$, or

$$|\Delta \eta_i| \leq \left(\frac{2\varepsilon}{\lambda_i} \right)^{1/2}. \quad (10)$$

Using this, we write $\delta \mathbf{m}$ in terms of the transformed parameters:

$$\begin{aligned} \delta \mathbf{m} &= \sum_{i=1}^N \sum_{j=1}^N S_{ij} \left[\frac{c_{\alpha i}}{\alpha_0} \eta_j h_i(z), \frac{c_{\beta i}}{\beta_0} \eta_j h_i(z), \frac{c_{\rho i}}{\rho_0} \eta_j h_i(z), \frac{c_{q i}}{q_0} \eta_j h_i(z) \right] \\ &= \sum_{j=1}^N \eta_j [g_j^{(1)}(z), g_j^{(2)}(z), g_j^{(3)}(z), g_j^{(4)}(z)], \end{aligned} \quad (11)$$

where

$$g_j^{(k)} = \sum_{i=1}^N c'_{ki} S_{ij} h_i(z), \quad (12)$$

and the primed c are given by scaling the original c factors: $c'_{ii} = c_{\alpha i} / \alpha_0$, etc. We may use the orthogonalized parameters η_i as data that provide linear constraints to the earth model, $\delta \mathbf{m}$, for subsequent inversion for 3-D structure. The 3-D structure is important because it can help us understand the sea-floor geology and because inhomogeneities cause mode-mode coupling and thus influence the redistribution of noise energy. In the present application, we do not have sufficient path coverage for such a tomographic analysis.

DAMPING

In this section, we develop the damping strategy for single-path models of more than one physical parameter. The basic idea is that there is a region around \mathbf{p}_{opt} where $F(\mathbf{p})$ satisfies the inequality $F(\mathbf{p}) - F(\mathbf{p}_{\text{opt}}) < \varepsilon$, and the preferred model in this region is the model with minimum model norm. We use the scaling factors α_0 etc. to define an appropriate metric in model space for multidimensional models. The formulation in

terms of uncorrelated parameters η_i easily allows us to find the optimal model, in the sense of a minimal model norm I defined as

$$\begin{aligned} I &\equiv \int |\delta \mathbf{m}(z)|^2 dz \\ &= \int \left[\left(\frac{\delta \alpha(z)}{\alpha_0} \right)^2 + \left(\frac{\delta \beta(z)}{\beta_0} \right)^2 + \left(\frac{\delta \rho(z)}{\rho_0} \right)^2 + \left(\frac{\delta q(z)}{q_0} \right)^2 \right] dz \\ &= \sum_{i=1}^N \sum_{j=1}^N \eta_i \eta_j G_{ij}, \end{aligned} \quad (13)$$

where

$$G_{ij} = \sum_{k=1}^4 \int g_i^{(k)}(z) g_j^{(k)}(z) dz.$$

We minimize I by changing the optimal model (given by $\boldsymbol{\eta}^{\text{opt}} = \mathbf{S}^T \mathbf{p}_{\text{opt}}$) to a minimum-norm model with $\boldsymbol{\eta} = \boldsymbol{\eta}^{\text{opt}} + \Delta \boldsymbol{\eta}$ under the constraint that F is equal to the maximum allowable misfit $F(\mathbf{p}_{\text{opt}}) + \varepsilon$, or

$$\Delta \boldsymbol{\eta}^T \mathbf{\Lambda} \Delta \boldsymbol{\eta} = \sum_{i=1}^N \lambda_i (\eta_i - \eta_i^{\text{opt}})^2 = \varepsilon. \quad (14)$$

With a Lagrange multiplier μ ,

$$\text{minimize: } \sum_{ij} \eta_i \eta_j G_{ij} + \mu \sum_i \lambda_i (\eta_i - \eta_i^{\text{opt}})^2.$$

The solution is found by solving

$$(\mathbf{G} + \mu \mathbf{\Lambda}) \boldsymbol{\eta} = \mu \mathbf{\Lambda} \boldsymbol{\eta}^{\text{opt}} \quad (15)$$

for $\boldsymbol{\eta}$ in an iterative way with different values of μ until (14) is satisfied. Using $\mathbf{p} = \mathbf{S} \boldsymbol{\eta}$, we return to untransformed parameter space.

SCHOLTE WAVES

This strategy will now be applied to invert the records from the THUMPER experiment in southern California for a model consisting of S velocity β and shear damping Q_S . In this experiment, several shots were fired at the sea bottom at ranges between 0.4 and 3.5 km from receivers, yielding several records with clear interface waves out to a distance of 1.1 km (Schreiner *et al.* 1991). The explosions provide a structural model for studying the generation of interface waves at the ocean bottom, supposedly through scattering off small heterogeneities.

Fig. 1 shows the model that is representative of the ocean bottom at the site of the experiment (120.5°W, 32.6°N), near Site 469 of the Deep Sea Drilling Project (Yeats *et al.* 1981). This site is just off the Californian continental borderland. The water depth is 3800 m, which is deeper than the CCD. The borehole is in a small sediment-filled basin where the maximum sediment thickness is about 400 m. In the Scholte-wave experiment, we employed several ocean-bottom seismometers to record waves from small (2.2 kg) explosions. Fig. 2 shows the locations of the shots and instruments. The data from this experiment have been previously analysed using manual inversion of group velocities (Sauter, Dorman & Schreiner 1986; Schreiner *et al.* 1991). The model (Table 1 and Fig. 1) has a layer of sediments with a thickness slightly in excess of 200 m. It is overlain by a 3.8 km deep ocean. The sharp increase in Q_S at 6 m in this model corresponds roughly to a transition from a sand layer to a clay layer found at 7.5 m in DSDP Site 469 (Yeats *et al.* 1981).

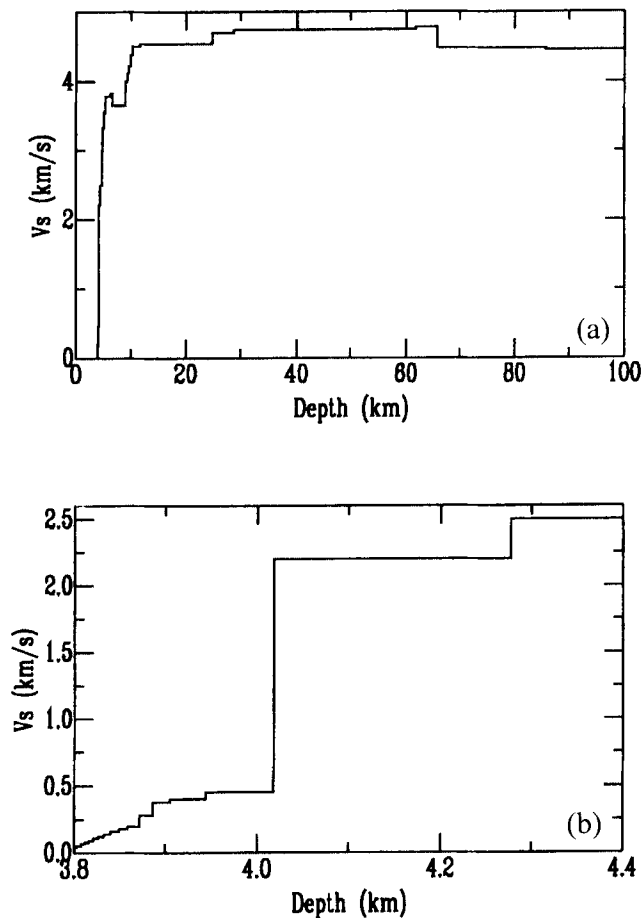


Figure 1. Background model for the ocean sediment at the site of the THUMPER experiment (120.5°W, 32.6°N). (a) shows the upper 100 km, including an oceanic layer of 3.8 km. (b) shows a blow-up of the top 600 m below the sea-bottom, which has the biggest influence on the waves discussed in this paper.

The phase- and group-velocity curves of the Rayleigh waves in this model show a distinctive pattern (Fig. 3). The lowest phase velocity in this curve belongs to the fundamental mode, sinking to values below 500 m s^{-1} near 0.5 Hz. At successively higher frequencies, the low curves of the fundamental-mode phase and group velocity are joined by curves of the higher modes. This is where the energy of the modes becomes trapped at the water-sediment interface. Phase and group velocities of the fundamental mode are well below 100 m s^{-1} for frequencies above 1 Hz, and the fundamental mode will be evanescent except perhaps at the top of the sediment layer where the S velocity is lower than the phase velocity. The higher modes may penetrate to depths as large as 80 m. These are known as Scholte waves (Scholte 1958). The phase-velocity diagram shows three more plateaus of almost constant phase velocity: one near 3700 m s^{-1} , corresponding to waves trapped in a slightly low S -velocity layer starting at a depth of 2.2 km, and one indicating penetration into the upper mantle with an S velocity of 4380 m s^{-1} . Below these two there is a plateau at 1500 m s^{-1} , which is the velocity of the P wave in the water layer and which illustrates the exotic nature of the Rayleigh waves in this model: as the frequency decreases from a very high value, a particular mode first escapes upwards from the interface into the water layer, and will have the character of

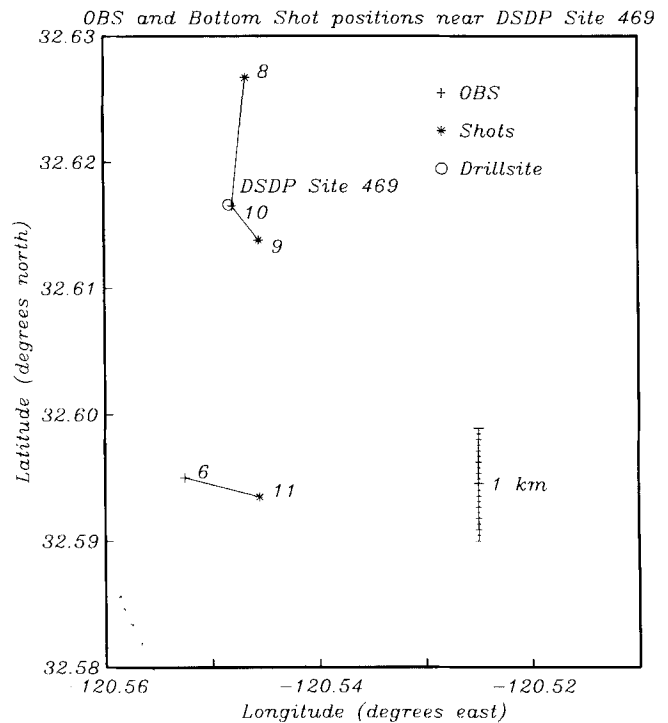


Figure 2. Locations of shots and OBSs for the THUMPER experiment.

Table 1. Sediment model below sea-floor.

Thickness (m)	α (m/s)	β (m/s)	ρ (kg/m ³)	Q_S	Q_S^{-1}
1	1500	30	1400	22	.0455
1.8	1500	40	1400	30	.0333
4.8	1500	50	1400	100	.0100
2.8	1500	70	1400	110	.0091
4.8	1500	80	1400	110	.0091
4.8	1500	90	1400	110	.0091
4.8	1500	110	1400	110	.0091
6.6	1500	120	1500	110	.0091
7.6	1500	140	1500	110	.0091
9.5	1500	160	1600	110	.0091
9.5	1500	180	1600	110	.0091
14.2	1500	200	1620	110	.0091
14.2	1500	280	1640	110	.0091
19.0	1500	380	1680	110	.0091
38.0	1500	400	1700	125	.0080
74.1	1500	450	1700	125	.0080
230.0	4400	2200	1920	125	.0080

an acoustic wave. However, as the frequency decreases further and the phase velocity increases such that the wave starts to penetrate the crust, the wave gains shear energy and eventually becomes a mantle Rayleigh wave. Note that the pattern of phase velocities is matched by the group velocities: phase-velocity plateaus correspond to extremes in group-velocity curves that line up (see Fig. 3). Consequently, the arrivals belonging to such plateaus should show little or no dispersion and can be identified as body waves.

The waveforms obtained in the THUMPER experiment illustrate the theoretical analysis remarkably well. Table 2 lists the shot times and Fig. 4(a) shows the three recordings at distances of 400, 595 and 1070 m. These were selected for the well-dispersed Scholte wavetrain visible at later times. The records are from three different shots; the recordings at 400 and 1070 m

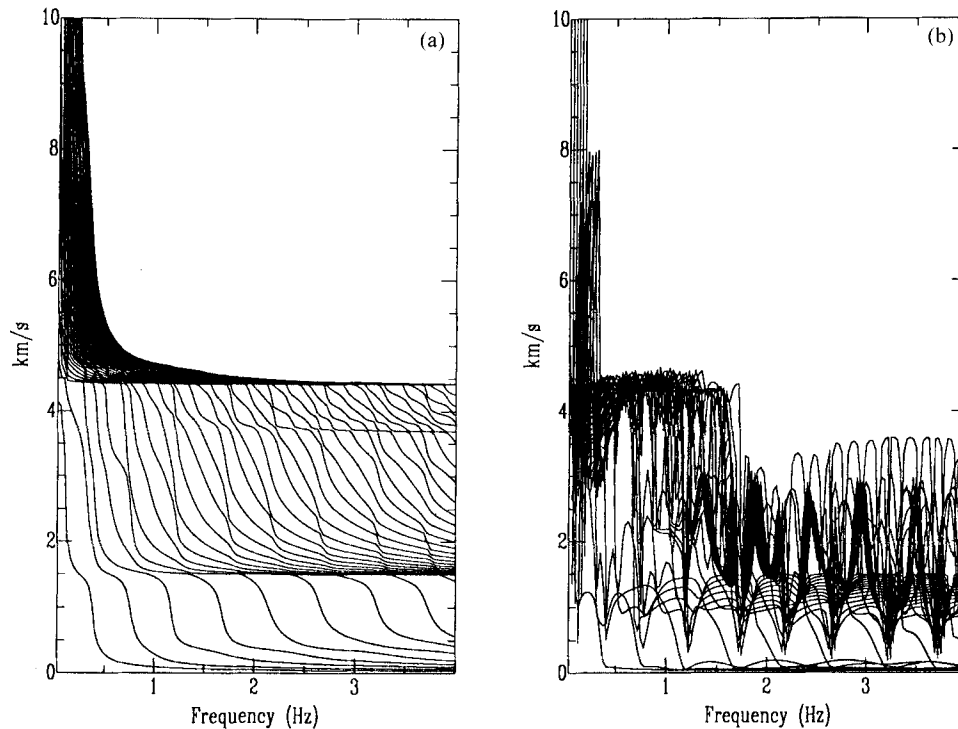


Figure 3. Rayleigh-wave phase (a) and group (b) velocities for the model shown in Fig. 1. Phase-velocity plateaus are visible near velocities corresponding to the water P velocity (1.5 km s^{-1}), the lower crustal S velocity (3.7 km s^{-1}) and the mantle S velocity ($\sim 4.5 \text{ km s}^{-1}$).

Table 2 Observed shots on March 25, 1984.

OBS	Shot time	distance(m)
6c	10:59:50	595
10a	7:59:59	1070
10b	8:59:50	400

were obtained from the same OBS. However, the three waveforms travelled different paths (Fig. 2). Some higher-mode energy is seen to arrive in front of the fundamental mode, for example between 6 and 8 s in record 10b (400 m). A wave reflected from the surface arrives near 5 s in all records. All three records were clipped at the start, which is evident in the low-passed data (Fig. 4b). A close examination of the water pulse shows that clipping is probably of less influence at the intermediate record (595 m). All data were converted to acceleration before inversion.

The 2 kg explosive sources used in the THUMPER experiment were not strong enough to generate deeply penetrating Rayleigh waves with appreciable energy, and the dominant signals we study in this section are the large-amplitude waves visible in Fig. 4(b), with group velocities below about 60 m s^{-1} . Inspection of the dispersion curves in Fig. 3 shows that, below 2.5 Hz, only the fundamental and the first four overtones contribute to arrivals in this time window. This was confirmed by a comparison of synthetic signals consisting of the fundamental mode and adding four and 40 overtones, respectively.

The exotic behaviour of the modes in this case poses a curious problem of non-linearity. The modes change character relatively quickly, as exhibited by the steep slopes of the phase-velocity curves in Fig. 3. Therefore, a minor change in the sedimentary layer velocity can change the wave character from

an interface wave with low phase velocity to an (acoustic) water wave with a phase velocity near to 1500 m s^{-1} . This explains the behaviour of the partial derivatives of phase velocity with respect to changes in β . It shows that an overall constant change of 1 m s^{-1} in S velocity in the sediment layers can induce a phase-velocity change as large as 100 m s^{-1} , an amplification by two orders of magnitude. In the period range of interest, the effect is small for the fundamental mode, but increases with mode number. Since our computation of $k_m(\omega; \mathbf{p})$ assumes linearity, care has to be taken when inverting waveforms. We found that a simple approach, in which phase-velocity changes larger than 20 per cent were simply cut off at that level in every iteration, avoided the most obvious numerical problems (such as perturbations to negative phase velocities). A second ‘outer loop’ iteration with re-computed eigenvectors showed that the non-linear effects in the inversion results are actually very small and can be ignored.

THE DETONATION SOURCE

To construct synthetic seismograms, a knowledge of the source spectrum is important. Unfortunately, no independent data on the spectral behaviour of each of the three sources is available. However, as we argue below, the time scale for the explosion—or equivalently the moment rate tensor—is short enough to be considered a delta pulse for all practical purposes. We shall make a theoretical estimate of the source strength (parameterized by the scalar moment) and check this for consistency among the three inverted paths.

In an underwater explosion, the explosive charge is rapidly converted into a bubble of gaseous detonation products (Cole 1948). The pressure within this bubble is much higher than the ambient water pressure, and the bubble increases rapidly

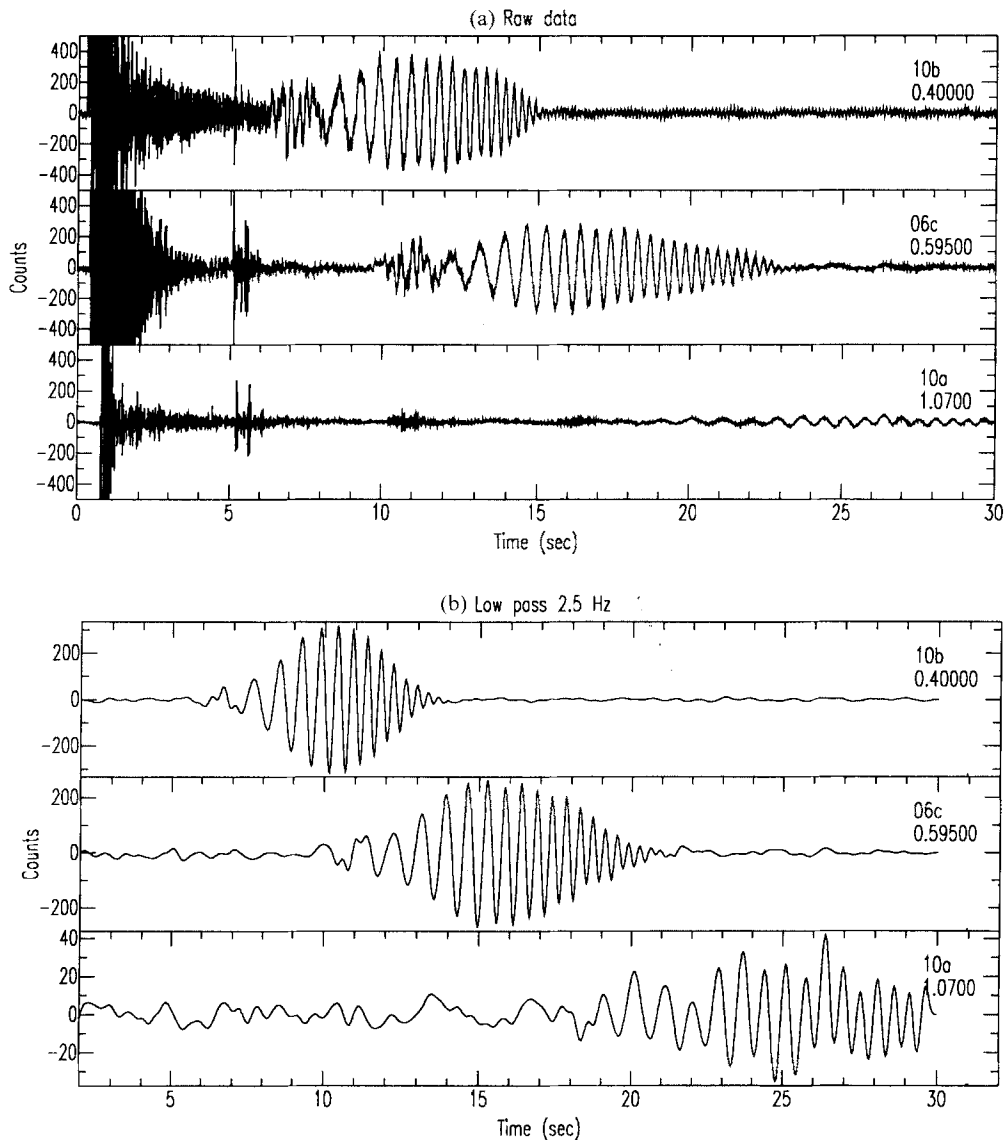


Figure 4. (a) Data for the three paths considered in this study, not corrected for the instrument response. (b) Data after applying a low-pass filter at 2.5 Hz.

in size. After the bubble has expanded to its equilibrium size, the momentum of the outward-moving water mass causes the bubble to expand to a size larger than that necessary to make the gas pressure equal to the hydrostatic pressure in the water, and the pressure deficit causes a restoring force which makes the bubble smaller. The size of the bubble thus oscillates for a few cycles. During this oscillation, the bubble radiates acoustic energy, especially when the bubble walls undergo large accelerations during the minima of the bubble size. As energy is radiated, the range of oscillation decreases, and the bubble volume approaches its equilibrium size at the ambient pressure.

Several time scales are important in underwater explosions. The first is that of the detonation itself. The velocity of detonation of TNT (trinitrotoluene) is about 6.9 km s^{-1} , and the radius of a 2.27 kg (5 lb) sphere of TNT is 0.069 m, so the time scale of the detonation process is about $0.1 \mu\text{s}$. The second significant time scale is the period of bubble oscillations: 2.9 ms from the theory of the adiabatic expansion of an ideal gas (Arons 1948).

The third significant time scale is that of the round-trip traveltime of an acoustic wave between the shotpoint and the sea surface. This separates the purely dynamic regime from that where the concept of hydrostatic pressure has significance. The fourth time scale is the time of the cooling of the detonation products and their dissolution into water. The time scale of the dissolution is a few minutes; see Fig. 3 of Hammer *et al.* (1994).

To model the low-frequency spectrum of an explosion, we need to calculate the moment, which is proportional to the volume change caused by the source. This volume is the difference between the volume initially occupied by the unexploded charge and the volume occupied by the combustion products at the end of the process. We are interested in the spectrum in the 0.3–3 Hz frequency range, since this is the range in which we observe Scholte waves. The time scale of interest is thus the 0.3–3 s range, much larger than the detonation and bubble oscillation time scales but smaller than the surface reflection and dissolution time scales. We can therefore treat the moment time dependence as a step function in time.

The theory of volume seismic sources is treated by Aki & Richards (1980), at the end of Chapter 3. They consider a spherical volume source of radius a as it undergoes a transformational expansion. For this case, the moment M is given by their eq. (3.34), which is

$$\mathbf{M} = \frac{4\pi}{3} a^3 \begin{bmatrix} \Delta p & 0 & 0 \\ 0 & \Delta p & 0 \\ 0 & 0 & \Delta p \end{bmatrix}. \quad (16)$$

Here, $\Delta p = (\lambda + \frac{2}{3}\mu)\Delta\theta$, where $\Delta\theta$ is the fractional change in volume.

For a shot of 5 lb (2.27 kg), the scale length from adiabatic theory is 0.309 m (Arons 1948). The equilibrium bubble radius is 0.62 times the scale length, so the equilibrium volume is 0.0296 m³.

The shots for this experiment were placed in pressure cases which were about half full. Since the explosive volume is 0.00138 m³ we will take v_0 to be 0.00276 m³. We take v_1 to be the equilibrium gas volume from ideal gas theory, i.e. 0.0296 m³.

In eq. (16), the term in front of the matrix is the volume of the source sphere, so the diagonal terms of the tensor have the form

$$\begin{aligned} M_{11} &= v \left(\lambda + \frac{2\mu}{3} \right) \Delta\theta \\ &= \kappa v \frac{\Delta v}{v} \\ &= \kappa(v_1 - v_0). \end{aligned}$$

We are using a source depth of 1 m within the sediments, where κ is 3.15×10^9 N t m⁻². Thus, the moment tensor is

$$\mathbf{M} = 7.62 \times 10^7 \begin{bmatrix} 1 & 0 & 0 \\ 0 & 1 & 0 \\ 0 & 0 & 1 \end{bmatrix}.$$

The adiabatic bubble theory is widely used for computing the relationship between bubble oscillation period and source size, but the measurements used for calibration were mostly taken at depths much shallower than the 3800 m depth of this experiment. For this reason, another independent, although also empirical, estimate of the bubble size was made.

In an explosion, the detonation wave compresses the solid explosive, moving along the solid Hugoniot in PV space. When detonation occurs, the locus in PV space was taken to move to the Chapman–Jouguet (C–J) point, which allows the minimum detonation velocity satisfying conditions for steady-state propagation of the detonation. From the C–J point, the isentrope of the detonation products of TNT was followed down to a pressure of 380 bars. These calculations were made using the Becker–Kistiakowski–Wilson (BKW) equation of state developed at Los Alamos Scientific Laboratory (Mader 1979). At 380 bars, the specific volume is 0.00945 m² kg⁻¹. This yields a gas volume of 0.02145 m³, a slightly smaller value than produced by the adiabatic theory. For reasons explained later, we used the larger value.

WAVEFORM INVERSION FOR THE S VELOCITY

For the weights adopted in eq. (5) we choose β_0 equal to 45 m s⁻¹, reflecting a 100 per cent *a priori* uncertainty of the S velocity near the top of the sedimentary layer, which decreases to a 25 per cent uncertainty at a depth of 50 m. The basis functions for $\delta\beta(z)$ allowed for linear interpolation with supports located at seven depth levels between 0 and 96 m, and at three more levels down to 1142 m depth. We chose $q_0 = 0.6$, also reflecting a very large *a priori* uncertainty of Q_S^{-1} . Perturbations to negative values of Q_S^{-1} are truncated at 0 to reflect infinite Q_S . The five basis functions for Q_S^{-1} peak at 0, 5, 13, 28 and 65 m depth. The damping factor ϵ was set at 1 per cent of the minimum value of the misfit $F(\mathbf{p}^{\text{opt}})$.

The (acceleration) amplitude spectrum for the data is mostly confined to the band between 1 and 2 Hz (Fig. 5). In this band, the fundamental mode has phase velocities between 99 and 55 m s⁻¹, with those of the first higher mode being between 301 and 98 m s⁻¹. This implies that the fundamental mode becomes evanescent at a depth of 20 m, and the first higher mode at 86 m in the background model.

The result of the inversion shows most of the velocity change to be confined to the upper 75 m of the sedimentary layer (Fig. 6). Although the changes of a few m s⁻¹ seem small, a 3 m s⁻¹ change near 2 m depth actually amounts to 7 per cent of the background velocity at that depth. Nevertheless, the model largely confirms the earlier model resulting from an analysis of fundamental-mode dispersion (Sauter *et al.* 1986; Schreiner *et al.* 1991). In particular, although the individual models differ in details, a gradient of about 2.8 m s⁻¹ m⁻¹ over the first 150 m of sediments seems a consistent feature for all three paths. The resultant phase fit is satisfactory for the whole wavetrain (Fig. 7), which is remarkable in view of the high frequencies involved. We shall discuss the misfit in amplitude in the next section.

We can obtain a quantitative idea of the resolving power by inspecting the effect of further damping on the final model. Slight misfits in phase show up if ϵ is raised to 10 per cent, but the change in $\delta\beta$ is small and generally below 0.5 m s⁻¹ in the well-resolved top 20 m (Fig. 8), and we estimate that the velocity is accurate to 0.5 m s⁻¹. The results of this test are also an indication that the conjugate gradient algorithm used in the non-linear stage effectively damps the model to the right level. Below 40 m depth, the velocity correction becomes very small with $\epsilon = 10$ per cent, an indication that we are losing resolving power. We conclude from this test that we have a good resolution down to 20 m, and satisfactory sensitivity to as far as 40 m. This is in agreement with the depth penetration of the higher modes at the signal maximum near 2 Hz, which for phase velocities near 100–150 m s⁻¹ become evanescent between 25 and 40 m depth.

INVERSION FOR THE Q MODEL

The greatest difficulty in fitting the amplitudes of the recorded wavetrain is caused by an initial imbalance between the low and high frequencies. Fig. 5 shows the spectrum for record 06c together with the initial synthetic, using the Q_S model shown in Table 1. Although there is a reasonable match in amplitude for frequencies between 2 and 2.4 Hz, the synthetic is less than half the observed amplitude at frequencies below 1.8 Hz. In

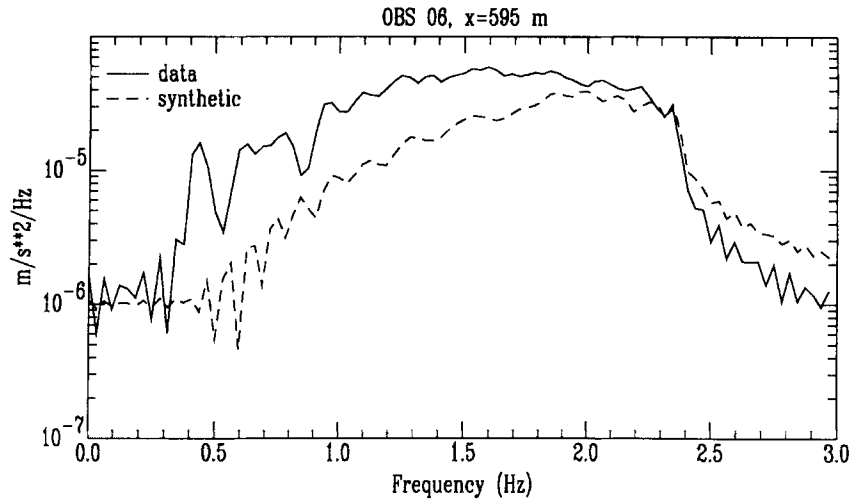


Figure 5. Acceleration amplitude spectra for record 06c (distance 595 m). The solid line denotes the data, the broken line the fit obtained using the Q model of Table 1 and a scalar moment of 7.6×10^7 N m.

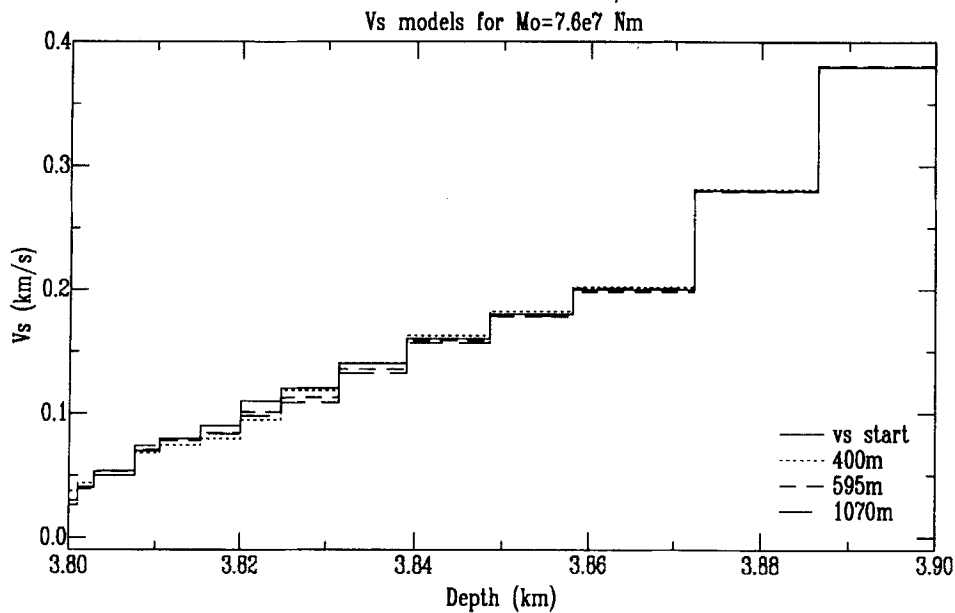


Figure 6. Models for the S velocity β .

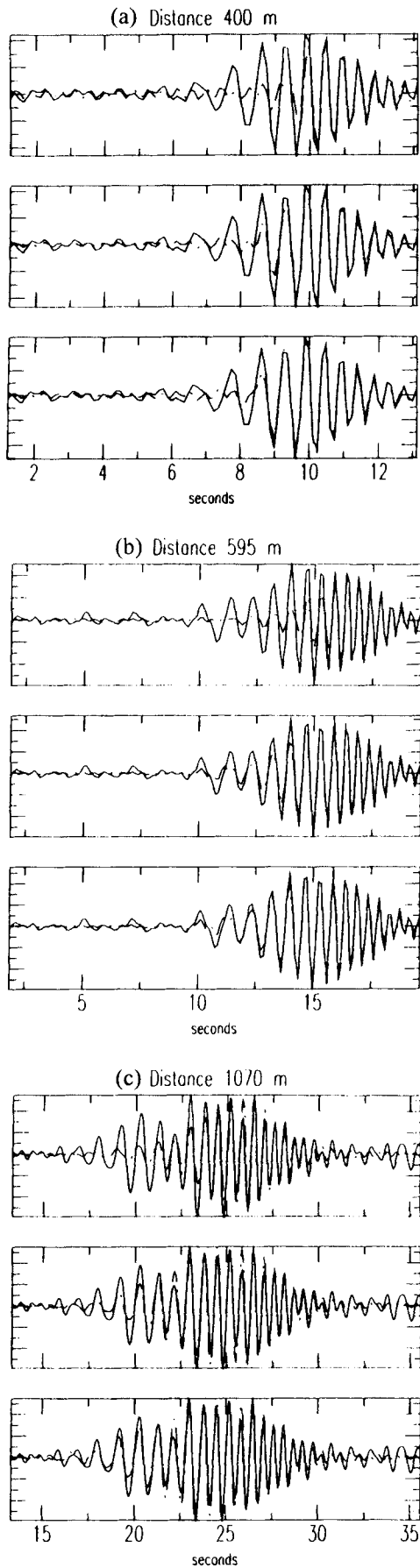
view of the very short time scale of the detonation (14 ms) it is not feasible to correct for the imbalance by modifying the Heaviside source time function with a finite rise time, which would have to be of the order of 0.5 s. Fig. 5 seems to indicate either that the low frequencies are damped too heavily, or that the source strength is underestimated by a factor of about 2, or a combination of these two options.

Although we might be able to compensate for an under- or overestimate of the scalar moment by changing the Q model at one particular range in a narrow frequency band, this becomes increasingly difficult as the frequency band widens, since the amplitude of a mode with quality factor $Q_n(\omega)$ is proportional to $\exp[-k_n(\omega)x/2Q_n(\omega)]/\sqrt{(k_n x)}$ and depends strongly on frequency through $k_n = \omega/c_n$. When we have more than one range x , consistency of the different models for Q_S^{-1} is a strong constraint on the scalar moment. We shall use this to test our theoretical estimate of the source strength.

In a first series of inversions, we kept the scalar moment

fixed at the theoretical value of 7.62×10^7 N m. The resulting models for Q_S^{-1} are shown in Fig. 9(b) for each of the three paths involved. The three paths show a reasonable agreement for the Q models, which differ by about 20 per cent. In all three cases, the Q_S^{-1} for depths in excess of 7.5 m are reduced to 0 or close to 0, indicating negligible loss for the Scholte waves in the frequency window that we consider. This is intuitively problematic, as the large hydrostatic pressure is fully compensated by the pore pressure in the clays, and some grain boundary sliding is to be expected. We shall discuss the resulting models more fully in a later section, but first we consider the possibility that our theoretical source strength is in error.

Figure 7. Waveform fits for the three paths considered. Within each part of the figure, top panel: $M_0 = 3.8 \times 10^7$ N m; centre panel: $M_0 = 7.6 \times 10^7$ N m; bottom panel: $M_0 = 11.4 \times 10^7$ N m.



There is some observational basis for the use of a smaller moment. Gilliam & Dorman (1990) reported that the bubble frequency and pressure waveforms observed from deep shots were consistent with a smaller charge size than was actually used. However, if an error in the scalar moment is responsible for the very low values of Q_S^{-1} below 7.5 m, it would have to be that we underestimated the moment. This is confirmed by the results of a second inversion with half the scalar moment (3.81×10^7 N m), shown in Fig. 9(a). We now see large differences between the models for Q_S^{-1} along the three paths. Such inhomogeneity is not to be expected over such short distances in this area. Also, the waveform fits in the top traces of Figs 7(a), (b) and (c) are less than satisfactory, as the amplitude fit has deteriorated greatly.

A third series of inversions was therefore done with the scalar moment increased by 50 per cent. Even though this is a large deviation from the theoretical prediction of the source strength, we feel we cannot casually reject this value since the spectrum as well as the waveforms show a very much improved fit, while the models for Q_S^{-1} remain compatible (Fig. 9c). An increase of source strength by 100 per cent not only is unlikely on theoretical grounds, it also does not remove the need for very low values of Q_S^{-1} : while showing synthetic amplitudes that are too high between 1.5 and 2 Hz, it still underestimates the observed spectrum near 0.5 Hz. The consistent discrepancy at the low-frequency end of the spectrum between the theoretical predictions and the observed values warrants further investigation of the behaviour of detonations at very low frequencies. We currently lack the necessary observational data to do this.

In the absence of more direct information of the source behaviour, we therefore propose that the scalar moment is in the range $7.8\text{--}11.4 \times 10^7$ N m. We are therefore led to conclude that the very low value of Q_S^{-1} in the clay layer (8 m in the inversion result, 7.5 at DSDP Site 469) is a real phenomenon. Although strictly speaking this source is outside the range of validity of the refined moment magnitude scale (Hanks & Kanamori 1979), this source moment corresponds to a moment magnitude of -0.63 to -0.74 .

The resulting models for Q_S^{-1} for these two options are shown in Table 3. The differences between the estimates in Table 3, which are of the order of 20 per cent for the top layers, reflect the uncertainty in the estimates of Q_S^{-1} . Zero values found in the clay layer are probably consistent with very small attenuation of the order of 0.003–0.005.

DISCUSSION

Despite the uncertainty in the source strength and the resulting attenuation models, we can draw some tentative conclusions regarding the attenuative mechanisms that are operating. Some of the early literature on attenuation in marine sediments centres around a controversy about the dominant dissipative mechanism: grain boundary friction or viscous loss due to pore fluid motion.

Hamilton (1972) compiled *in situ* measurements of attenuation in the kHz frequency band in marine sediments, including sands and clays off the coast near San Diego, but in a much shallower environment (< 1100 m). If his data between 1 and 1000 kHz can be extrapolated to 1 Hz, we find a compressional Q_P^{-1} of 0.028 for fine-grained sands, and 0.003 for fine-grained clayey silts. Hamilton prefers intergrain friction as the attenuative mechanism in sands, but it is obvious that this cannot

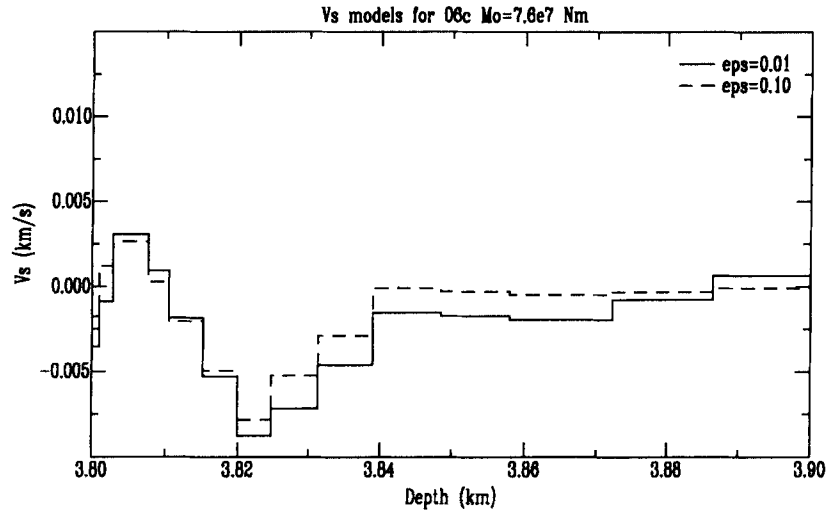


Figure 8. Comparison of the S -velocity model along path 06c using damping values ϵ of 1 per cent (solid line), and 10 per cent (broken line).

be the only cause of energy loss. Boltzmann's superposition principle can be used to express the attenuation coefficients in terms of the imaginary components of the elastic moduli (which are frequency-dependent). For P waves, we define (O'Connell & Budiansky 1978)

$$2Q_P = \frac{\text{Re}(\alpha)}{\text{Im}(\alpha)} - \frac{\text{Im}(\alpha)}{\text{Re}(\alpha)},$$

or, for $\text{Im}(\alpha) \ll \text{Re}(\alpha)$:

$$Q_P^{-1} = \frac{\text{Im}(\kappa) + \frac{4}{3}\text{Im}(\mu)}{\text{Re}(\kappa) + \frac{4}{3}\text{Re}(\mu)}, \quad (17a)$$

$$Q_S^{-1} = \frac{\text{Im}(\mu)}{\text{Re}(\mu)}. \quad (17b)$$

If $\text{Im}(\kappa) \approx 0$, as it would be if there were no loss associated with viscous absorption through pore-water movement and only grain boundary sliding were operative, then Q_S^{-1} for the sand would be as high as 50; this would imply that no shear waves could propagate, in obvious disagreement with our observations. Indeed, Winkler, Nur & Gladwin (1979) observe that grain boundary friction is important for high ($>10^{-6}$) strain, and they do consider fluid flow to be important. A grain boundary friction mechanism would operate to attenuate both P and S waves, but it might well be dominated by the viscous flow mechanism for the P waves, since κ dominates μ and $\text{Im}(\mu)$ is obviously an order of magnitude smaller than μ itself. Again for sands, Prasad & Meissner (1992) find that $\text{Im}(\kappa)$ is an order of magnitude larger than $\text{Im}(\mu)$. If this result can be generalized to our experiment, it would imply a dominant loss due to flow for compressional waves, as Hamilton (1972) observed, although with only very small attenuation since $\text{Re}(\kappa) \gg \text{Re}(\mu)$. We therefore are led to conclude that both pore-fluid motions and grain boundary sliding contribute to energy loss in the sand layer.

The fact that attenuation decreases sharply from the sand to the clay layer can be understood if we assume that grain boundary sliding is the dominant mechanism operating in the

clay. Hamilton (1971) discusses the properties of marine clays in detail. In contrast to sand particles, cohesion can be strong in a clay, and the S velocity is expected to be higher. However, the S velocity found below 8 m is still less than 100 m s^{-1} (Fig. 6), and the reason for the drop of attenuation to the low levels shown in Table 3 is not intuitively obvious. We conjecture that it is the change in grain size that brings the relaxation times for grain boundary sliding outside the period range of our experiment, thereby significantly reducing the energy loss.

Karato & Spetzler (1990) assume a rate of sliding proportional to the shear stress to derive an expression for the relaxation time τ :

$$\tau = d/\mu B_S, \quad (18)$$

where B_S is the proportionality coefficient or sliding mobility, d the grain size and μ the shear modulus. We have no information on the magnitude of B_S . We could, however, assume that τ for sands must be in the same period range as the Scholte waves, since the damping mechanism is most effective in this layer. This allows us to make a rough estimate of B_S . Setting $\tau = 1 \text{ s}$ gives $B_S \approx 3 \times 10^{-11} \text{ m s}^{-1} \text{ Pa}^{-1}$ for $d = 50 \text{ }\mu\text{m}$, and $\mu = 1.7 \times 10^6 \text{ Pa}$. For clays with $d = 5 \text{ }\mu\text{m}$, and $\mu = 6.8 \times 10^6 \text{ Pa}$, τ decreases to 0.024 s. We conjecture that the spread of relaxation times is small enough to bring the mechanism outside the frequency band of Scholte waves for the clay layer, effectively reducing the attenuation to almost zero.

CONCLUSION

Our study has shown a clear potential for waveform fitting on 0.5–2.5 Hz Scholte waves for local studies. The procedure is robust even for interface waves, where linear perturbation theory locally breaks down. Waveform fits of the fundamental mode provide a means to determine the local S velocity in the top layer of the sediments down to about 20 m with a precision of the order of 0.5 m s^{-1} . The direct comparison of waveforms in the time domain provides a check on the occurrence of wave scattering or multipathing that may remain undetected in dispersion studies. The successful fitting of the mode sums

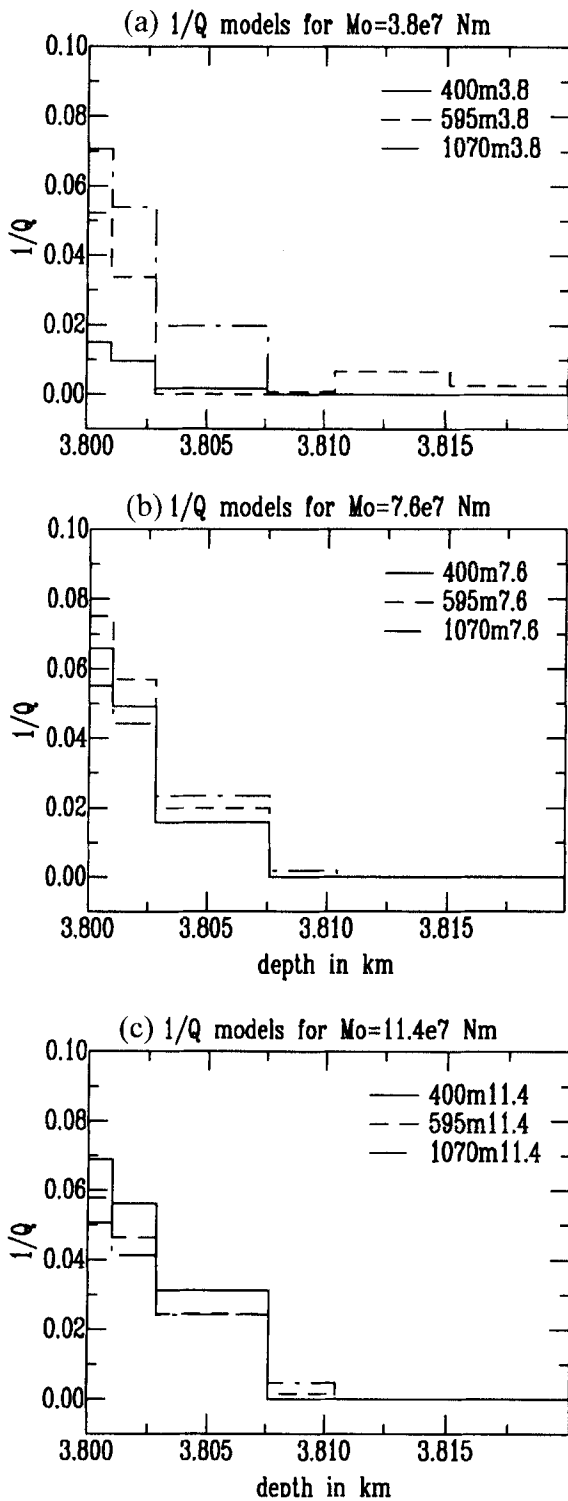


Figure 9. Models for Q_S^{-1} . (a) $M_0 = 3.8 \times 10^7$ N m, (b) $M_0 = 7.6 \times 10^7$ N m, (c) $M_0 = 11.4 \times 10^7$ N m.

to observed records confirms the earlier diagnosis of Schreiner & Dorman (1990) and Dorman & Schreiner (in preparation) that much of the ocean-floor noise consists of low-order harmonics of Scholte waves. The method can be used for determination of Q_S^{-1} as a function of depth, although a direct estimate of the source strength using a hydrophone at close range will significantly improve the precision of Q_S^{-1} estimates.

Table 3(a). Q_S^{-1} for $M_0 = 7.6 \times 10^7$.

Depth(m)	10b 400m	06c 595m	10a 1070m
1	.066	.075	.055
2	.049	.057	.044
6	.016	.020	.023
8	.000	.000	.002
12	.000	.000	.000

Table 3(b). Q_S^{-1} for $M_0 = 11.4 \times 10^7$.

Depth(m)	10b 400m	06c 595m	10a 1070m
1	.069	.058	.051
2	.056	.046	.041
6	.031	.024	.024
8	.000	.002	.005
12	.000	.000	.000

ACKNOWLEDGMENTS

LMD acknowledges support from the Office of Naval Research under contract N00014-90-J-1275 and thanks C. Mader for explaining how explosions really work. Bob Whitmarsh and Neil Frazer read an early version of the manuscript and their comments were greatly appreciated. GN received support from NSF grant EAR 9204386.

REFERENCES

- Aki, K. & Richards, P.G., 1980. *Quantitative Seismology*, Vol. 1, Freeman, New York, NY.
- Arons, A.B., 1948. Secondary pressure pulses due to gas globe oscillation in underwater explosions. II Selection of adiabatic parameters in the theory of oscillation, *J. acoust. Soc. Am.*, **20**, 277–282.
- Bromirski, P.D., Frazer, L.N. & Duennebieber, F.K., 1992. Sediment shear Q from sediment OBS data, *Geophys. J. Int.*, **110**, 465–485.
- Caiti, A., Akal, T. & Stoll, R.D., 1991. Determination of shear velocity profiles by inversion of surface wave data, in *Shear waves in marine sediments*, pp. 557–565, eds Hovem, J.M. et al., Kluwer, Dordrecht.
- Cole, R.H., 1948. *Underwater Explosions*, Princeton University Press, Princeton, NJ.
- Dorman, L.M., Schreiner, A.E. & Bibee, L.D., 1991. The effects of shear velocity structure on seafloor noise, in *Shear waves in marine sediments*, pp. 239–245, eds Hovem, J.M. et al., Kluwer, Dordrecht.
- Dziewonski, A.M. & Hales, A.L., 1972. Numerical analysis of dispersed seismic waves, in *Seismology: surface waves and earth oscillations* (Methods in Computational Physics, Vol. 11), pp. 39–85, ed. Bolt, B.A., Academic Press, New York, NY.
- Gilliam, D. & Dorman, L., 1990. Modeling deep underwater explosions, *EOS, Trans. Am. geophys. Un.*, **71**, No. 43, 1372.
- Hamilton, E.L., 1971. Elastic properties of marine sediments, *J. geophys. Res.*, **76**, 579–604.
- Hamilton, E.L., 1972. Compressional-wave attenuation in marine sediments, *Geophysics*, **37**, 620–646.
- Hammer, P.T.C., Dorman, L.M., Hildebrand, J. & Cornuelle, B.D., 1994. Jasper seamount structure: seafloor seismic refraction tomography, *J. geophys. Res.*, **99**, 6731–6752.
- Hanks, T.C. & Kanamori, H., 1979. A moment magnitude scale, *J. geophys. Res.*, **84**, 2348–2350.
- Jensen, F.B., Kuperman, W.A., Porter, M.B. & Schmidt, H., 1994. *Computational ocean acoustics*, AIP Press, New York, NY.
- Karato, S. & Spetzler, H.A., 1990. Defect microdynamics in minerals and solid state mechanisms of seismic wave attenuation and velocity dispersion in the mantle, *Rev. Geophys.*, **28**, 399–421.

- Mader, C.L., 1979. *Numerical modeling of detonations*, Univ. Calif. Press, Berkeley, CA.
- Nolet, G., 1990. Partitioned wave-form inversion and 2D structure under the NARS array, *J. geophys. Res.*, **95**, 8513–8526.
- Nolet, G., van Trier, J. & Huisman, R., 1986. A formalism for nonlinear inversion of seismic surface waves, *Geophys. Res. Lett.*, **13**, 26–29.
- O'Connell, R.J. & Budiansky, B., 1978. Measures of dissipation in viscoelastic media, *Geophys. Res. Lett.*, **5**, 5–8.
- Prasad, M. & Meissner, R., 1992. Attenuation mechanisms in sands: laboratory vs. theoretical (Biot) data, *Geophysics*, **57**, 710–719.
- Rauch, D., 1980. Experimental and theoretical studies of seismic interface waves in coastal waters, in *Bottom-Interacting ocean acoustics*, pp. 307–327, eds Kuperman W.A. & Jensen, F.B., Plenum, New York, NY.
- Sauter, A.W., Dorman, L.M. & Schreiner, A.E., 1986. A study of sea floor structure using ocean bottom shots, ocean seismo-acoustics, low-frequency underwater acoustics, in *NATO Conf. Series IV*, **16**, pp. 673–681, eds Akal, T. & Berkson, J.M., Plenum, New York, NY.
- Scholte, J.G.J., 1956. On seismic waves in a spherical Earth, *Meded. en Verhand. KNMI*, **65**, 5–55.
- Scholte, J.G.J., 1958. Rayleigh waves in isotropic and anisotropic elastic media, *Meded. en Verhand. KNMI*, **72**, 9–43.
- Schreiner, A.E. & Dorman, L.M., 1990. Coherence lengths of seafloor noise: effects of ocean bottom structure, *J. acoust. Soc. Am.*, **88**, 1502–1514.
- Schreiner, A.E., Dorman, L.M. & Bibee, L.D., 1991. Shear wave velocity structure from interface waves at two deep water sites in the Pacific Ocean in *Shear waves in marine sediments*, pp. 231–238, eds Hovem, J.M. et al. Kluwer, Dordrecht.
- Seibold, E. & Berger, W.H., 1993. *The Sea Floor*, Springer-Verlag, Berlin.
- Winkler, K., Nur, A. & Gladwin, M., 1979. Friction and seismic attenuation in rocks, *Nature*, **277**, 528–531.
- Yeats, R.S. et al. 1981. Site 469: Base of the Patton Escarpment, *Init. Repts DSDP 63*, US Govt Printing Office, Washington, DC.